Lawrence Berkeley National Laboratory
LBL Publications

Title

Binary pseudo-random array (BPRA) for inspection and calibration for cylindrical wavefront interferometry

Permalink

Authors

Munechika, K
Rochester, S
Chao, W
et al.

Publication Date

DOI

Copyright Information

Peer reviewed

Binary pseudo-random array (BPRA) for inspection and calibration for cylindrical wavefront interferometry

K. Munechika[a], S. Rochester[b], W. Chao[c], I. Lacey[d], C. Pina-Hernandez[a], Kaito Yamada[a],
V. V. Yashchuk[d], M. P. Biskach[e], A. Numata[f], and W. W. Zhang[e]

[a]HighRI Optics, Inc., 5401 Broadway Terr, St. 304, Oakland, California 94618, USA;
[e]Rochester Scientific, LLC, 2041 Tapscott Avenue, El Cerrito, CA 94530, USA
[c]Center for X-ray Optics, Lawrence Berkeley National Laboratory, Berkeley, CA 94720, USA;
[d]Advanced Light Source, Lawrence Berkeley National Laboratory, Berkeley, CA 94720, USA;
[e]NASA Goddard Space Flight Center, 8800 Greenbelt Road, Greenbelt, MD 20771 USA;
[f]KBR, Inc., Space Engineering Division, 7701 Greenbelt Road, Greenbelt, MD 20771 USA

ABSTRACT

High-accuracy metrology is vitally important in manufacturing ultra-high-quality free-form mirrors designed to manipulate X-ray light with nanometer-scale wavelengths. However, surface topography measurements are instrument dependent, and without the knowledge of how the instrument performs under the practical usage conditions, the measured data contain some degree of uncertainty. Binary Pseudo Random Array (BPRA) "white noise" artifact are effective and useful for characterizing the Instrument Transfer Function (ITF) of surface topography metrology tools and wavefront measurement instrument. BPRA artifact contains features with all spatial frequencies in the instrument bandpass with equal weight. As a result, power spectral density of the patterns has a deterministic white-noise-like character that allows direct determination of the ITF with uniform sensitivity over the entire spatial frequency range. The application examples include electron microscopes, x-ray microscopes, interferometric microscopes, and large field-of-view Fizeau Interferometers. Furthermore, we will introduce the application of BPRA method to characterizing the ITF of Cylindrical Wavefront Interferometry (CWI), by developing the BPRA artifact which matches the radius of curvature of the cylindrical wavefront. The data acquisition and analysis procedures for different applications of the ITF calibration technique developed are also discussed.

Keywords: calibration, instrument transfer function, ITF, power spectral density, PSD, interferometric microscopes, binary pseudo-random, test standard, aberration, surface metrology

1. INTRODUCTION

High-accuracy metrology is vitally important in the optimal manufacture and use of ultra-high-quality free-form mirrors designed, for example, for space x-ray telescopes to manipulate x-ray light with nanometer-scale wavelengths. Due to the shorter wavelength, requirements on the surface figure (shape) and finish (roughness) of x-ray mirrors are many orders of magnitude more stringent than for visible-light optics. Additionally, because practically all optical materials are transparent to x-ray light at normal incidence, grazing incidence is used to achieve acceptable reflectance. This results in additional complications for metrology: To get a reasonable optical aperture, the X-ray mirrors are significantly elongated in the tangential direction and must be strongly aspherical with the tangential radius of curvature (ROC) larger than that of the sagittal direction by a few orders of magnitude. Correspondingly, the metrology integrated into x-ray mirror manufacturing must ensure the accuracy of optical surface fabrication on the sub-nanometer level over large area (on the scale of a meter and even more) strongly aspherical optical elements with the sagittal ROC on the order of a meter and less, whereas the tangential ROC can reach a few hundred meters. The absence of the required metrology is the major limitation of the modern technology used for fabrication of x-ray mirrors. As an adage says, "If you can't measure it, you can't make it."

Metrology technology has not kept up with the advancement in fabrication technologies. It is the deficiencies in the metrology, rather than in the fabrication technologies that primarily limits the optical quality. For example, the micro-stitching metrology used in the elastic emission machining (EEM) deterministic nano-fabrication process [1-3] produces aberration errors that depend on the surface curvature. Such errors are often transferred into the optical surface topography

*Corresponding author: km@highrioptics.com; phone 1-(800) 470-7902; https://highrioptics.com/

of x-ray mirrors, where they result in quasi-periodic errors in the surface height and slope [4]. Therefore, advanced integrated metrology is key for the improvement of optical manufacturing technology, urgently needed for fabrication of free-form aspherical x-ray mirrors with moderately and strongly curved shapes, such as paraboloids, ellipsoids, hyperbolas, diaboloids, etc.

1.1. Challenges with performing metrology for Mid-Spatial Frequency

There are several different techniques currently in use for metrology with x-ray mirrors. Interferometric microscopes, widely used for surface roughness metrology over middle spatial frequencies, are capable of measurements only over a very limited surface area of not more than approximately 10 x 10 mm2. Micro-stitching interferometry [5] is extremely slow and inaccurate in application to strongly sagittally curved and large space x-ray mirrors. High accuracy measurements of the x-ray mirror surface slope variations along the tangential direction are possible with surface slope profilometry (SSP) [6], but the resulting trace is essentially one dimensional (1D) and does not reflect the overall surface quality of the mirror. Moreover, the accuracy of SSP in measurements along the sagittal direction with small ROC is unacceptably low.

A technology that appears capable of performing the required metrology with large X-ray mirrors is cylindrical wavefront interferometry (CWI), realized, for example, with a large aperture Fizeau interferometer equipped with a cylindrical transmission reference (CTR), or, in an advanced realization, with a conical computer-generated hologram (CCGH) diffraction element [7-9]. To enable high-accuracy CWI surface metrology, it is vital to overcome the problems related to cylindrical wavefront distortion due to the limited manufacturing quality of the CTR (or CCGH) itself and the light source built into the interferometer. The most powerful approach to solve, or at least significantly mitigate, this problem is to combine the measurements with high-precision calibration of the metrology tool in the spatial domain (to characterize the systematic errors, such as geometrical aberrations also known as 'retrace' or 'propagation' errors – see Sec. 1.2) and in the spatial frequency domain (to characterize the spatial resolution). If thorough calibration is available, it can be used to correct the measurements via sophisticated data processing to mitigate the spurious effects of the tool's resolution limitations and systematic errors [6,10]. In previous work [11-13], we have established a calibration technique for plane wavefront interferometry (PWI) based on binary pseudo-random array (BPRA) calibration standards specially designed and fabricated to ensure high-accuracy measurement of the instrument transfer function (ITF) of broad spectrum of metrology tools [14-16]. However, for CWI, the strong asymmetry of the wavefront of the sampling light beam in the tangential and sagittal directions will require an adaptation of this technique.

1.2. Retrace errors

It has been long recognized that high-accuracy surface shape measurements using conventional laser Fizeau interferometers are affected by a specific systematic error, known as retrace (propagation) error [17-20]. The retrace error appears due to the aberrations in the optical system of the interferometer and the surface under test (SUT) related to the optical path difference (OPD) of the rays from the SUT and those from the interferometer's reference surface. In the case of the conventional interferometric optical testing of plane and spherical mirrors in a single-fringe-interference arrangement with the plane and spherical transmission references, the retrace error may be negligible. However, when the SUT is aspherical, as desired, for example, for focusing x-ray mirrors, the SUT-reference OPD can strongly perturb the measured interference fringe pattern, leading to non-negligible retrace error, that can be as large as 100 nm peak-to-valley (PV).

Figure 1 illustrates the importance of the retrace error even in the case of PWI measurements with a slightly curved cylindrical x-ray optic with ROC of 120 meters. In Fig. 1, the retrace error is seen as a residual (after detrending of the best-fit cylindrical surface) height variation of ~120 nm PV that is unchanged when the SUT is measured in the direct (Fig. 1a) and in the flipped (Fig. 1b) orientations. The fact that this observed variation is spurious is confirmed by measurements of the same optic with a surface slope profiler OSMS [21] available at the Advanced Light Source (ALS) X-Ray Optics Laboratory (XROL) [22] that show a residual surface error on the level of only a few nanometers (Fig. 1c).

For highly aspherical x-ray optics designed for two-dimensional (2D) manipulation of x-rays, such as paraboloidal mirror shells for space x-ray telescopes [26,27] or diaboloidal mirrors [28,29] for beamline applications at x-ray facilities, the sagittal and tangential curvatures of the optical surfaces can differ by a few orders of magnitude with significant variation along the mirror. Surface characterization of such aspherical optics can be performed with Fizeau interferometry in the CWI mode [7,9,30] or with specially developed refractive nulls [24,25], but systematic errors such as retrace error are potentially even more significant.
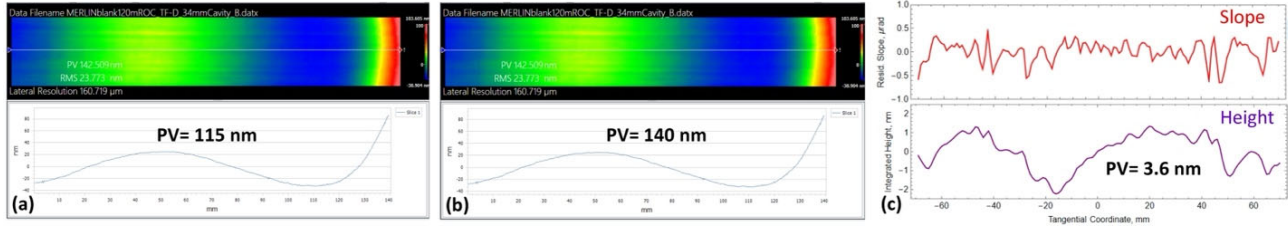
Figure 1. Illustration of the retrace error contribution to the PWI measurements with a cylindrical x-ray optic with ROC of 120 meters. The residual (after detrending of the best-fit cylindrical surface) height variations as measured with the SUT (a) in the direct and (b) in the flipped orientation; the corresponding PV variations are 115 nm and 140 nm, respectively. (c) The results of measurements of the same optic with the ALS XROL OSMS slope profiler OSMS [21] in the slope (the top plot) and in the height (the bottom plot) domains; the surface error measured with the OSMS is 3.6 nm (PV).

The retrace error in a particular measurement depends on the shape, tilt, and focus (lateral position) of the SUT (see, for example, Ref. [23] and references therein). Thus, for effective calibration, an analysis must be made of measurements taken over a range of surface positions and curvatures. To allow this, we report the innovation of patterned calibration artifacts with variable shape – i.e., patterns imprinted on thin substrates that can be bent over a range of ROCs to supply a complete set of calibration data (discussed further below). This will allow thorough calibration with minimal expense for the artifact fabrication.

2. BINARY PSEUDO RANDOM TEST ARTIFACTS

X-ray mirrors are complex and expensive optical elements with challenging technical requirements on surface quality specified over an extremely broad spatial wavelength range, from a fraction of the x-ray wavelength up to the total size of the optic (from sub-nanometer to as large as one meter and even more). The metrology provides three-dimensional surface profile data that serves as feedback used to correct for surface figure and finish errors in the deterministic polishing process. The quality and cost of the optics directly depends on the accuracy and speed of the integrated metrology. The current state of the art of mirror fabrication technology for x-ray mirrors is expensive and time consuming. Neither under-specification nor over-specification are desirable; under-specification would undermine the telescope performance, and over-specification would further increase the cost of already expensive mirror manufacturing. Therefore, the ability to assess the high accuracy and high-efficacy metrology is key for further improvement of optical fabrication and lowering the cost of x-ray optics.

As mentioned above, we will address this issue using the methodology we have previously developed for application in PWI metrology [11-13]. To adapt the methodology to CWI-based instruments, specially designed test samples, including BPRA standards was created along with the development of analytical methods and software for data processing. The technique will allow the user to experimentally measure the ITF of the CWI-based instruments with high accuracy, and then deconvolve the ITF from measured data, reducing the effects of instrument aberrations and systematic errors and yielding additional (super) resolution beyond the nominal resolution of the metrology tool [6]. For example, it was recently demonstrated that deconvolution can reveal a few times more information in the height profile of a 1D chirped grating [10].

The ITF of a given metrology tool describes, as a function of spatial frequency, the amplitude and phase factors imparted to measured surface data due to the optical aberrations and limited resolution of the instrument [31]. The ITF is one of the most comprehensive quantitative characteristics of metrological instruments. The key for the ITF characterization involves test samples with surface topography patterned as a 1D BPR grating (BPRG) or a 2D BPRA [10-16]. The algorithm for the random pattern was originally developed by LBNL in collaboration with National Instituted for Standards and Technology (NIST) [13]. These are effectively "white-noise" topography, which would result in a flat spatial-frequency response (power spectral density, PSD) when measured by an ideal instrument. For the metrology tool in question, the observed deviation from a flat PSD is a measure of the ITF (**Error! Reference source not found.**c).

This technique has been applied to a broad spectrum of metrology tools and demonstrated its effectiveness for electron, X-ray, and visible-light microscopes [10,14,15], as well as for large-aperture Fizeau interferometers [11-13]. A range of BPRA samples with smallest feature size from 1.5 nm up to dozens of microns are now available, as shown in **Error! Reference source not found.**. In 2015, the technology was recognized with a R&D 100 Award.
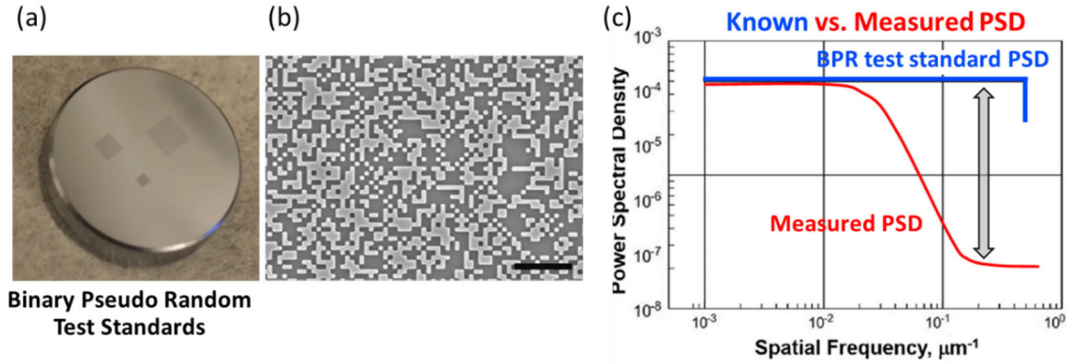
Figure 2. (a) Photograph of a binary pseudo random test standard fabricated on a flat Si substrate. Each square pattern is a BPRA patterns with various minimum feature sizes. The sample is designed for high–mid spatial frequency characterization. (b) Scanning electron micrograph of a section of BPRA pattern. The scale bar is 1 µm. (c) Comparison between the known (ideal) flat PSD of the BPRA vs. the PSD of the BPRA standard perturbed due to the tool's limited resolution (for illustration, the result of simulation is shown). The difference between the BPRA-inherent vs. the 'measured' PSDs describes the sensitivity loss of the metrology instrument of interest and is a measure of the instrument transfer function.
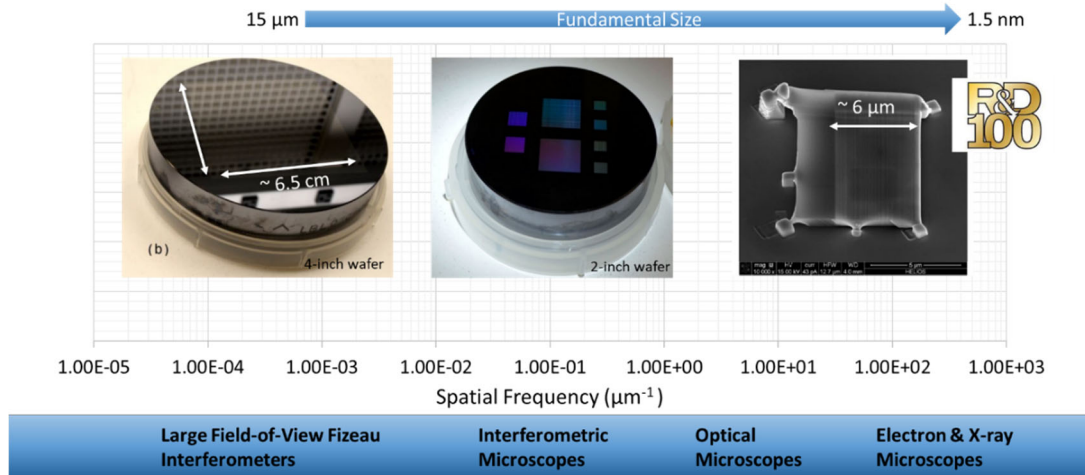
Figure 3. Several BPRA test samples designed, fabricated, and tested for a variety of metrology tools, including Fizeau interferometers, interferometric microscopes, and scanning probe and atomic force microscopes. The fundamental sizes of the arrays range from 1.5 nm to 15 µm.

BPRA test standards are fabricated using high-resolution electron beam lithography or contact lithography, followed by plasma etching into the substrate, typically silicon. The fabrication process inherently produces errors such as non-90 degrees sidewall angles and rounding of the corners. The fidelity of the patterns is characterized using a few different tools, including scanning probe microscopy, scanning electron microscopy, and interferometric microscopes. In our previous work [32], we have studied the effects of fabrication imperfections, such as rounded sidewalls, on the inherent PSD of a BPRA. **Error! Reference source not found.** shows the few elements of model BPRA's with different degrees of the rounding simulating the real case scenario of the fabrication process in use.

The simulated PSD spectra in **Error! Reference source not found.**b shows that a deviation from the ideal PSD (the horizontal straight line) occurs when the corners are significantly rounded. However, for all the studied cases, the deviation of the inherent PSD from the ideal white-noise like spectrum appears mainly over spatial frequencies far above the desired (application) spatial frequency range of the standard, corresponding to the size of the BPRA smallest element. **Error! Reference source not found.**c shows the scanning electron microscope image of a cross section of the real (fabricated) BPRA, after passing the initial quality tests. The fabrication process is optimized until the rounding is minimal and does not affect the calibration properties of the standard.
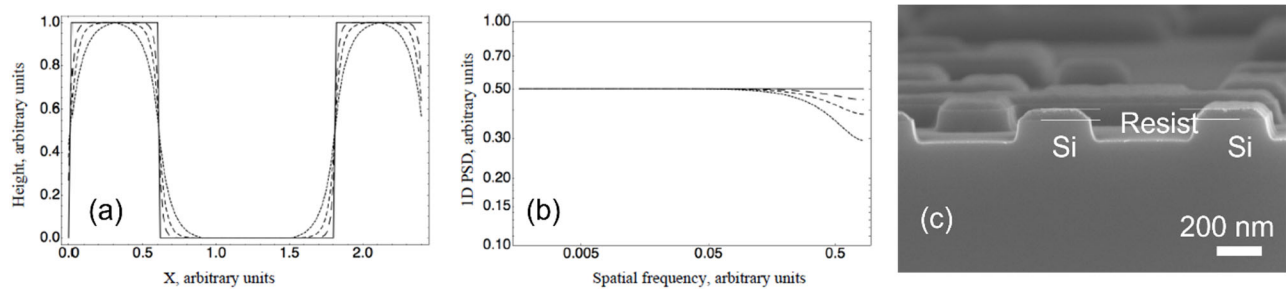
Figure 4. (a) One dimensional height profiles of a few smallest elements of the model BPRA with different degrees of rounding. The rounded edges approximate fabrication imperfections of a "real" BPRA. (a) 1D PSDs calculated for the BPRAs corresponding fabrication imperfections. A feature of the BPRA samples is that the deviation of the inherent PSD from the ideal white-noise like spectrum appears over the spatial frequencies far above the desired (application) spatial frequency range of the standard, corresponding to the size of the smallest element. (Figure adapted from Ref. [32]) (c) A SEM cross section image of the fabricated BPRA pattern into a Si wafer. The electron beam resist is remaining on top of the pattern. The side wall shows only a small deviation from the perfect 90-degree side wall.

We are now working to extend the use of the BPRA-based methodology beyond the plane-wave application, to Cylindrical Wavefront Interferometry. The prototype BPRA test standards are designed and fabricated to match the cylindrical wavefront, and data-processing software was developed to analytically model the ITF of the CWI-based tools, where the sampling periods are significantly different in the two orthogonal directions. Extension of our analytical procedure and software to surface reconstruction based on the modeled ITF in the case of the asymmetrical sampling will solve the problem of accounting for and mitigating the tool's imperfections in the final (processed/reconstructed) metrology data. The accuracy and resolution of the measured data will be greatly increased.

3. DEVELOPMENT OF TEST STANDARDS ON CYLINDRINCAL SUBSTRATES

The specifications for the BPRA pattern dimension, pattern area, and cylinder ROC were selected based on the cylindrical wavefront Fizeau interferometry setup available at NASA Goddard Space Flight Center (GSFC). Performing lithography on non-planar and highly curved surfaces is challenging as lithography tools are not normally designed to accommodate non-planar substrates. We initially used nanoimprint lithography as it is suitable for fabricating nano and microstructures with high fidelity and at low cost.

3.1. Selection of design parameters based on NASA's CWI

NASA's experimental setup scheme for the cylindrical wavefront measurement is shown in **Error! Reference source not found.**. We selected the cylindrical substrate with ROC of 34.4 mm. The BPRA design has a minimum feature size of 2.5 μm to characterize the ITF over low-to-mid spatial frequencies. Checkerboard patterns were also fabricated to evaluate the degree of distortion in the test pattern (due to the cylindrical substrate) and recorded image (due to cylindrical wavefront distortion).

3.2. Fabrication process development

Performing lithography on top of a non-planar surface is a challenging task. Electron beam lithography is normally a good choice as a high-resolution direct write technique, but it is not suitable in this case due to the substrate's high curvature. Based on the BPRA design and the substrate ROC choice, nanoimprint lithography is a promising approach. The basic process for the nanoimprinting is shown in Fig.6. The basic steps are to spin-coat the nanoimprint resist with a uniform thickness, apply the flexible mold, cure (i.e., harden) the resist, then detach the mold. In this scheme, nanoimprint resist will take the shape of the intended design (e.g., checkerboard or BPRA). Finally, a thin metal layer is applied, to make the surface reflective for optical measurement. They key here is to control the "Residual (polymer) Layer" (RL) to be uniform so as not to introduce any distortions to the surface curvature.

For the process development, we used a BPRA design with a minimum feature size of 1200 nm and pattern area of ~ 5 x 5 mm^2. We selected a NIL resist, MR-NIL210, with a relatively low viscosity to better control the uniformity of the resist. **Error! Reference source not found.**a shows a photograph of the BPRA sample after the nanoimprint process is applied, using the PDMS as the nanoimprint mold material. The patterned area is within the white square. Although the quality of

the nanoimprint needs optimization, the 2D BPRA patterns are still visible as shown in Fig. 7b. This substrate was used for the optical characterization as discussed below.
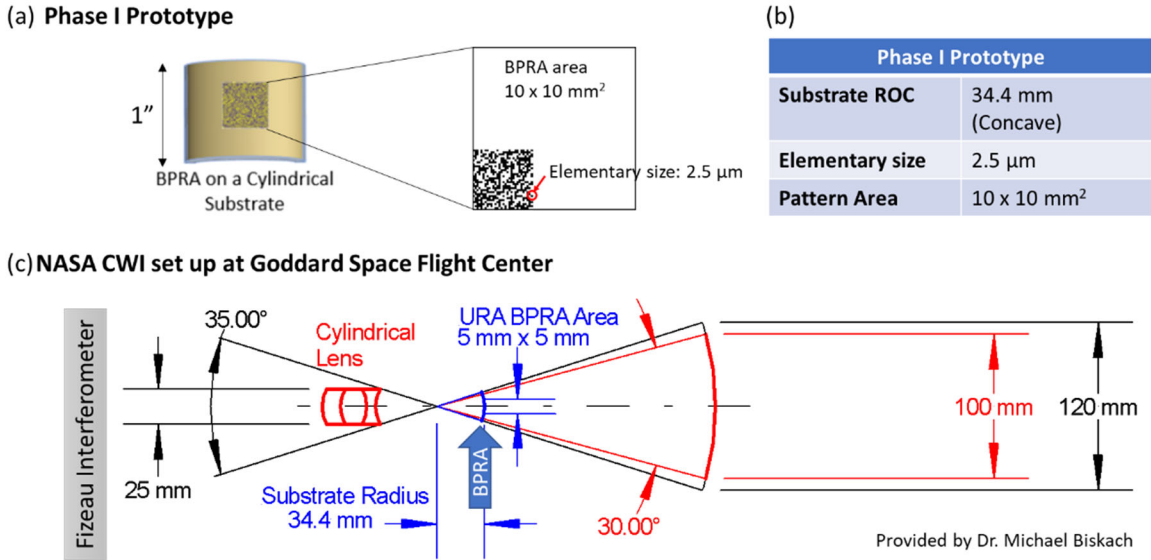

Figure 5. (a) Illustration of the prototype BPRA test artifact on a cylindrical substrate. (b) a table of design parameters optimized to characterize the CWI setup at NASA Goddard Space Flight Center, (c) A scheme of the CWI setup at NASA. The blue arrow marked with "BPRA" indicates the placement of the fabricated BPRA test artifact.
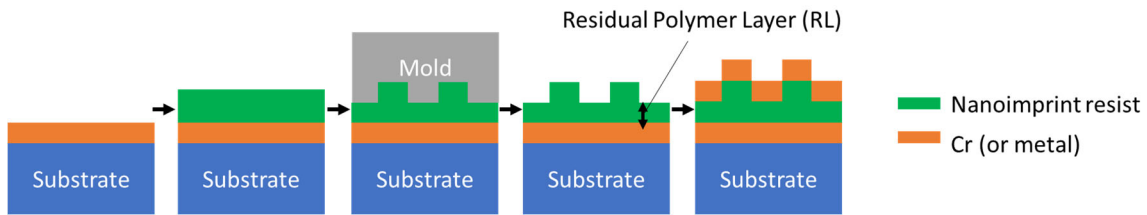
Figure 6. Nanoimprint process flow. The substrate is drawn as a planar substrate for simplicity. The actual sample is a cylindrical lens with ROC 34 mm.
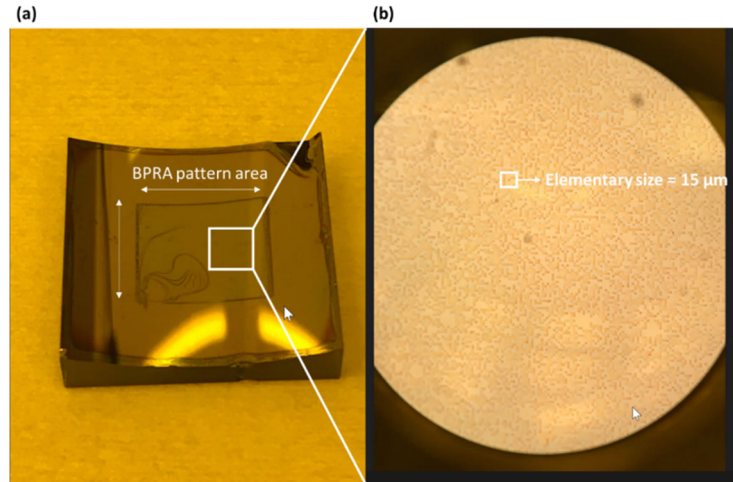
Figure 7. (a) Photograph of the BPRA sample on a concave cylindrical substrate after nanoimprint is performed. The BPRA pattern is clearly visible (b). The elementary size of the pattern (i.e. min feature size) is 15 μm.

3.3. BPRA test artifact with "adaptive" ROC

To enable a full field-of-view calibration of a CWI setup, an alternative process for fabrication of a high quality BPRA and checkerboard test samples needed to be explored. Instead of solid cylindrical substrates, we evaluated using flexible (bendable) flat Si wafers with sub-millimeter thickness. The key advantage of the flexible Si is that it be bent freely to achieve the ROC of interest and can be processed as a normal "flat" silicon, without the challenges of curved substrates. The biggest challenge may be the fragility of the substrate; they require careful handling and require a stable mounting mechanism is also needed. Our recent tests have shown that a suitable Si wafer with the thickness of 100 μm can be easily bent to the radius of curvature of 100 mm and even smaller, shown in Figure 8.
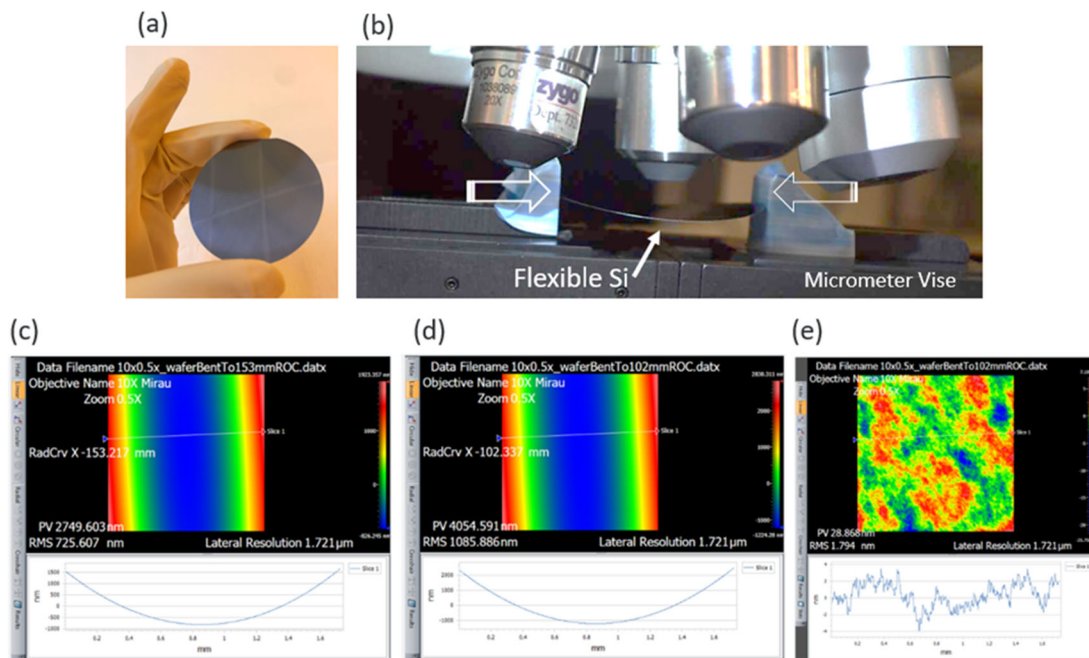

Figure 8. (a) Flexible Si wafer with 100 μm thickness. (b) Photograph of a Si wafer mounted onto a micrometer vise. Using a micrometer, it is possible to freely bend the wafer. The surface height topography of the 100-μm-thick Si substrate bent to the

cylindrical shape with ROC of (c) ~153 mm and (d) 102 mm as measured with the ZYGO NewView^{TM}-9000 interferometric microscope equipped with 10× objective and 0.5× zoom lens. (e) The residual height variation of the raw wafer with the best-fit curvature detrended with roughness of ~ 1.8 nm (RMS).

4. OPTICAL CHARACTERIZATION USING INTERFEROMETRIC MICROSCOPE AT ADVANCED LIGHT SOURCE

Currently, the ALS XROL is not capable of CWI metrology with test samples of cylindrical shape. However, the high-resolution microscope measurements are useful for development and optimization of the nanolithography process capable of fabrication of the BPRA test samples on a strongly curved cylindrical substrate. The developed test samples were characterized with the ALS XROL ZYGO NewView^{TM}-9000 interferometric microscope. The experimental arrangement of the microscope located in the XROL clean room is shown in Figure 9.

Besides providing fabrication feedback, the microscope measurements allow us to test the sample functionality as an ITF calibration standard for the microscope itself, when the sample design is appropriate for this tool. We also tested the flexible sample, described in Section 3.3. In order to bend the patterned wafer, we use a simple approach depicted in Figure 10b consisting of gently bending the wafer around a cylindrical base. In order to press the wafer, we use a permanent magnet and two magnetic steel bolts as the pressing rods. This simple design has provided an almost perfect cylindrical shape of the sample with the convex ROC of ~ 124 mm. In spite of the relatively low surface quality and, correspondingly, the cost of the wafer, the sample has a clear HR BPRA topography as seen in the high-resolution image in Figure 10d.
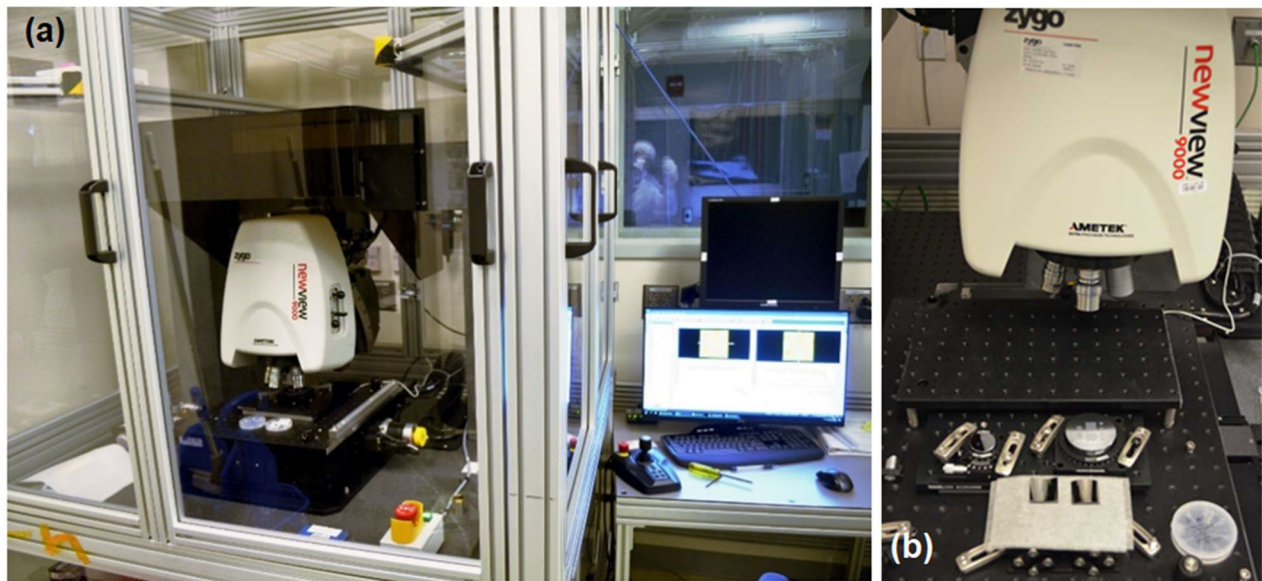

Figure 9. (a) Experimental arrangement of the ZYGO NewViewTM-9000 interferometric microscope located in the clean-room of the ALS X-Ray Optics Laboratory (XROL) [22]. The microscope is placed on a floating granite table surrounded with a plastic hutch. This arrangement ensures low sensitivity of the setup to airflow, vibrations, and the residual variation of the room temperature (on the level of ± 30 mK). (b) An enlarged view of the microscope showing two BPRA samples fabricated on concave and convex cylindrical substrates with the ROC 34.4 mm.
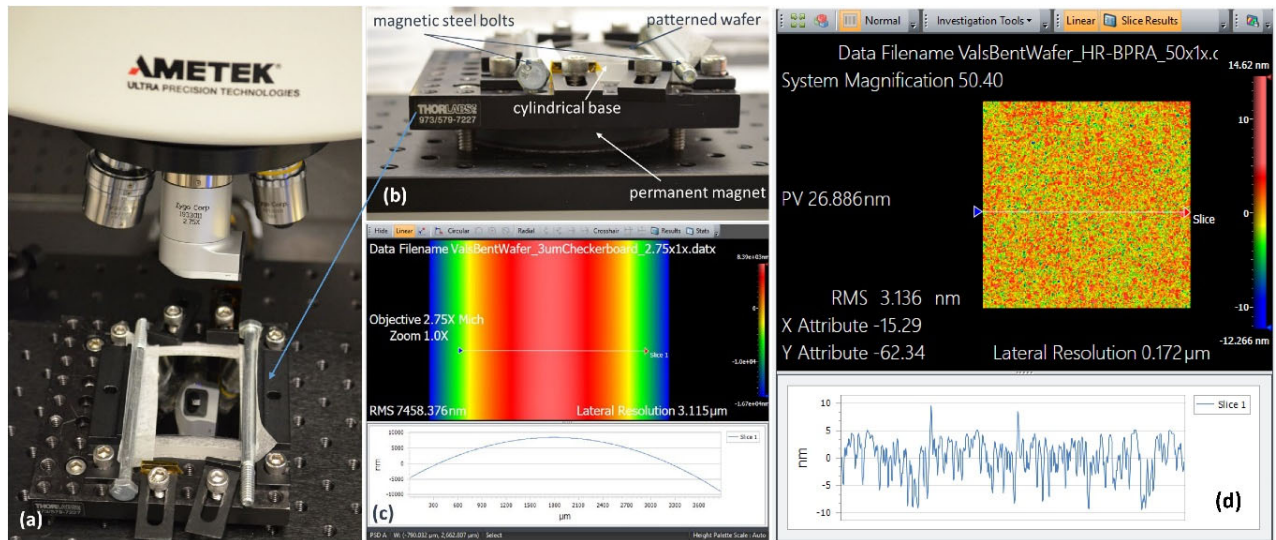
Figure 10. (a) Experimental arrangement of the ZYGO NewViewTM-9000 microscope for ITF calibration with the HR BPRA test sample on magnetically assisted bendable wafer. (b) Assembly of the bent HR BPRA sample with the convex ROC of ~ 124 mm. (c) The low resolution measurement of the ROC with the microscope equipped with 2.75x objective at 1x zoom (lateral resolution of ~ 3.1 µm). (d) High resolution (50x objective / 1x zoom, the measurement pixel size of 172 nm) image of the HR BPRA topography.

The result of the ITF calibration of the microscope equipped with the 20x objective at 0.5x zoom in shown in Figure 11. In this arrangement, the tool's measurement pixel size is 873 nm, twice larger than the fundamental size of the HR BPRA pattern. As shown in Ref. [33], this ratio is close to the optimum for the ITF calibration with the HR BPRA standards. The power spectral density (PSD) depicted in Figure 11b and evaluated from the height distribution (Figure 11a) measured with the 400-nm HR BPRA test artifact is the measure of the ITF of the microscope in the measurement arrangement.

In the PSD data in Figure 11, there is a noticeable difference between the 1D PSD distributions in two orthogonal directions, along and across the cylinder's axis of the bent wafer. Additional tests with a similar 400 nm HR BPRA sample but fabricated on a significantly more curved convex cylindrical substrate (ROC 34.4 mm) have allowed us to conclude that the observation is an artifact of the measurement, probably related to the low surface quality of the bent wafer seen in Figure 11 as the middle spatial frequency variation.
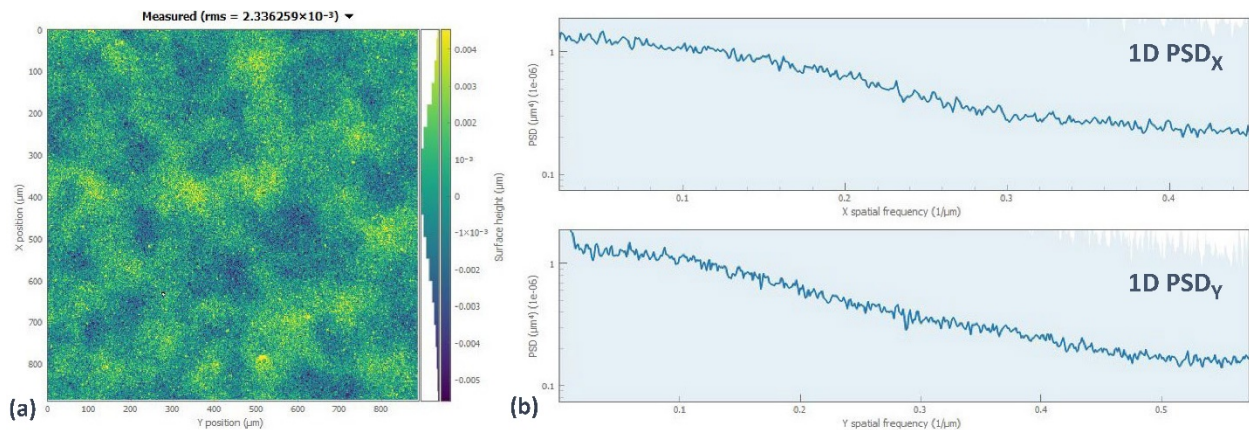

Figure 11. (a) The height topography of the HR BPRA test sample on the magnetically assisted bendable wafer as measured with the ZYGO NewViewTM-9000 microscope equipped with 20x objective at 0.5x zoom (the measurement pixel size is 873 nm). (b) The 1D power spectral densities of the height topography in plot (a): 1D PSDX and 1D PSDY correspond to the directions along and across of the cylinder's axis of the bent wafer.

5. CWI CHARACTERIZATION USING NASA'S TOOL

Figure 12 depicts the experimental arrangement of the proof-of-principle measurements performed at the NASA GSFC Metrology Laboratory with the 15-µm HR BPRA test sample on the concave cylindrical substrate with ROC of ~34.5 mm.
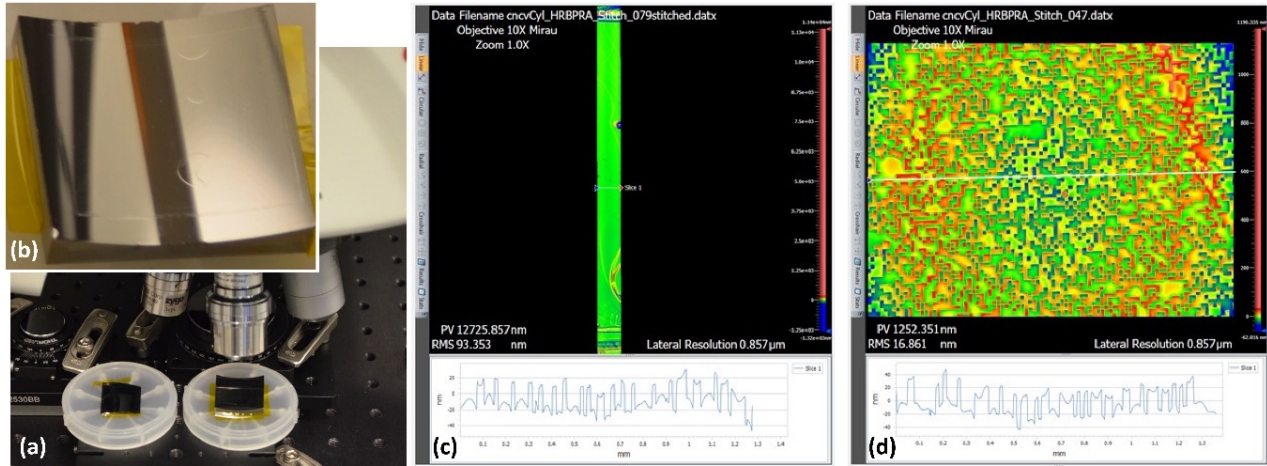

Figure 12. Characterization at the ALS XROL of the 15-µm HR BPRA test sample on the cylindrical substrate (ROC 34.5 mm) supplied to the NASA GSFC. (a) The sample as placed for measurements with ZYGO NewViewTM-9000 microscope equipped with 10x objective at 1x zoom (the measurement pixel size is 857 nm). (b) An enlarged view of the sample; the HR BPRA pattern of about 20 mm x 20 mm can be seen at the samples surface central area. (c) The height topography along central line parallel to the cylinder axis as measured by stitching together 78 overlapping fields of view. (d) A single pattern topography measurement within the stitched region, to show the pattern detail.
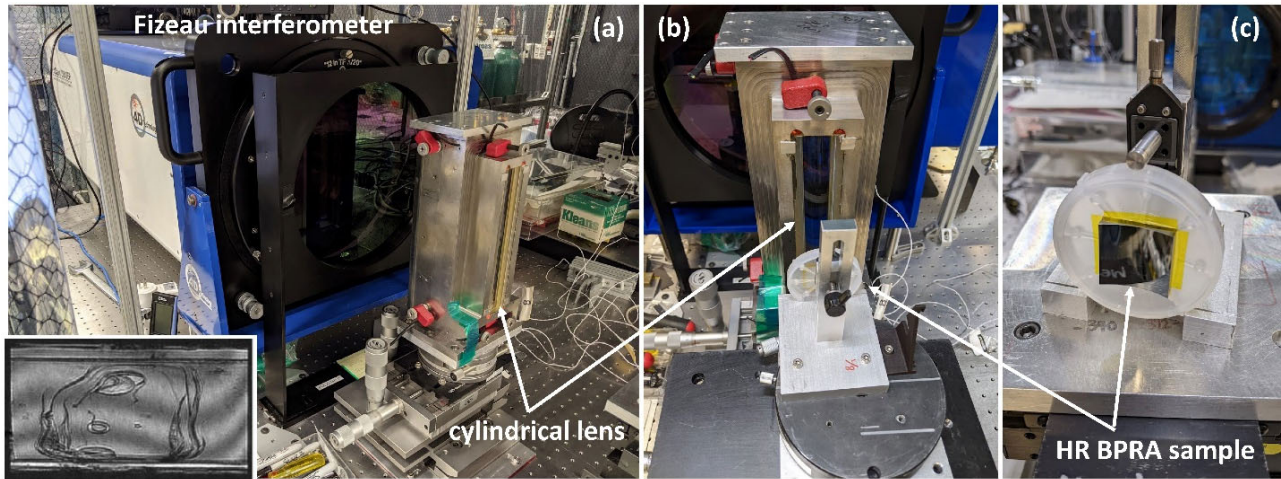

Figure 13. Experimental arrangement of the proof-of-principle measurements performed at the NASA GSFC with the 15-µm HR BPRA test sample on the concave cylindrical substrate. (a) The GSFC Fizeau interferometer equipped with an original and unique cylindrical lens. (b) The CWI measurement arrangement with the BPRA sample placed in the front of the cylindrical lens. (c) The BPRA sample as mounted on a rotation and alignment stage.

The unique large-aperture Fizeau interferometer (Figure 13a) has a built-in plane transmission reference. In order to form a cylindrical wavefront, an additional three-element cylindrical lens is used as a null element [25]. During alignment, the BPRA sample taped to the plastic box (Figure 13c) is mounted on the rotation and alignment stage (Figure 13b) that allows precision alignment of the BPRA pattern with respect to the cylindrical wavefront. The alignment criterion is the minimum possible number of fringes in the interference image shown in the inset in Figure 13a). Measurements taken at different

settings of the interferometer focus were provided to the ALS XROL for data processing and analysis. For the preliminary exploration of the data, we used the ZYGO™ Mx software. Figure 14 illustrates the data processing with the ZYGO™ Mx software.
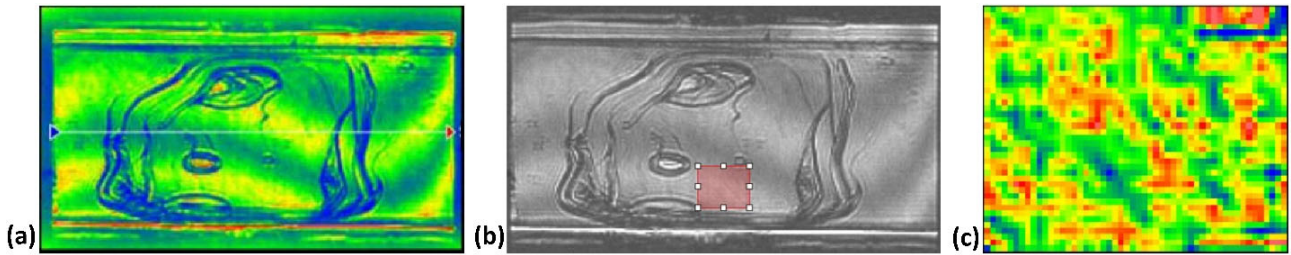

Figure 14. (a) The height variation as measured with the NASA GSFC CWI tool over the surface area of 20 mm x 20 mm. (b) The mask (the orange square) used for cropping of the data when processed with the ZYGO™ Mx software. (c) The height variation over the masked (cropped) area.

For measurements with the NASA GSFC CWI tool, a square aperture of 20 mm x 20 mm was placed in front of the sample. This allows a rough calibration of the effective pixel dimensions, which are different in the vertical and horizontal directions, as the image is magnified in the horizontal direction by the cylindrical lens. The ZYGO™ Mx software is not capable of accounting for non-square pixels. As the result, the square area measured is seen as a rectangular image (Figure 14a). As mentioned above, the surface of the sample has low-frequency spatial irregularities that are a result of the fabrication process. Nevertheless, the height variation over the area cropped with the mask, depicted in Figure 14b, has a clear HR BPRA pattern topography (Figure 14) that is useful for resolution (ITF) calibration of the tool. Figure 15 and Figure 16 summarize the results of application of PSD processing to the height data recorded with the different focus settings, where the 1D PSD are evaluated over the entire field-of view (Figure 15 and 16) over the masked area shown in Figure 14b.
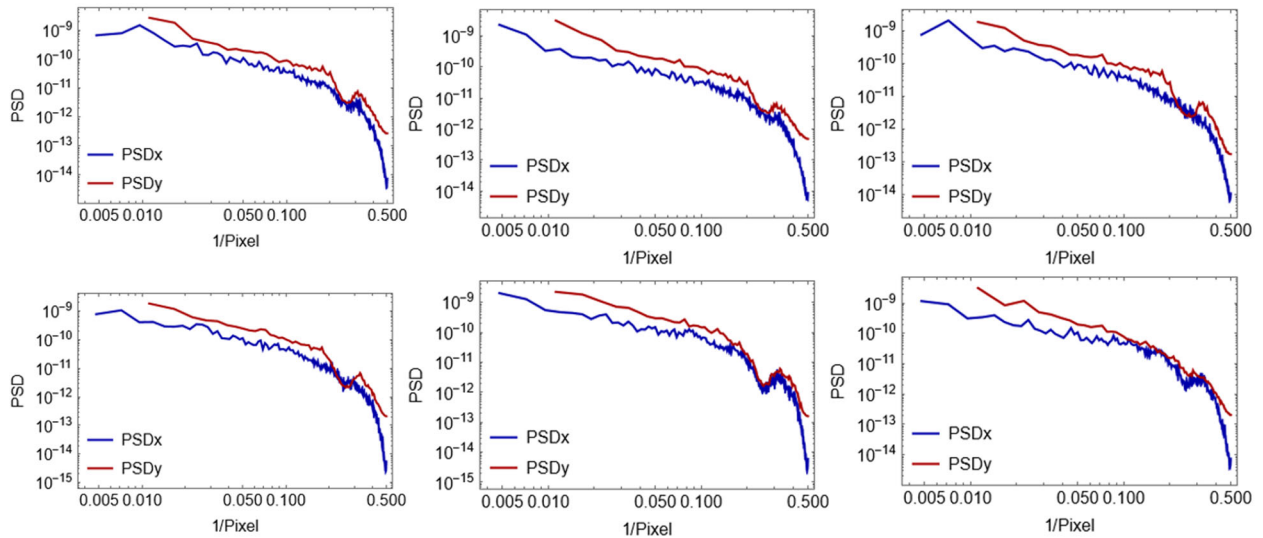

Figure 15. The results of application of PSD processing to the height data recorded with the NASA GSFC CWI tool at different focus settings. The 1D PSD distributions are evaluated over the entire field of view in *Error! Reference source not found.*b. A noticeable feature of the 1D PSD distributions is the characteristic dips appeared near the high spatial frequency cutoff of the PSD spectra. For more detail, see discussion in the text.
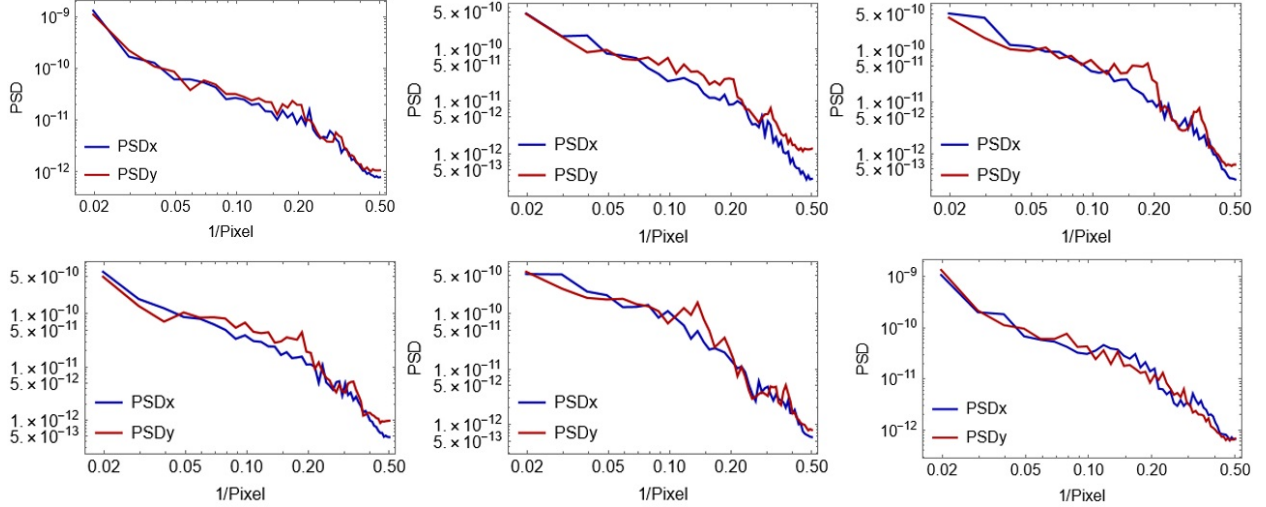
Figure 16. The results of application of PSD processing to the height data recorded with the NASA GSFC CWI tool at different focus settings. The 1D PSD distributions are evaluated over the masked areas as shown in Figure 14b.

A notable feature of the 1D PSD distributions is the characteristic dips that appear at some focus settings near the high spatial frequency cutoff of the PSD spectra (between 0.2 and 0.3 pixel-1 in Figure 16).

As shown in Ref. [13], the appearance of such PSD dips is a signature of non-optimal interferometer focus. For plane wavefront interferometry [13], the optimal foci in both directions are achieved at the same focus setting. As we can see in Figure 15 and 16, this is not the case for the CWI tool under testing where the dips in the PSDx and PSDy distributions are observed at different focus settings. This observation can be thought of as evidence of the problem with the CWI tool's design using the external cylindrical null lens.

Concluding this section, we emphasize that the proof-of-principle-tests of the GSFC CWI tool performed with a relatively low-quality prototype HR BPRA test sample already allowed us to get very important information about the tool's performance. Improvements in the sample quality is currently work in progress. Note also that the frequency units used in Figure 15 and Figure 16 are 1/pixel, and in these units the PSDx and PSDy distributions have the same cutoff frequencies. However, as discussed above, the effective pixel sizes are different in the x and y directions, and so the cutoff frequencies in physical spatial frequency units are different. This is shown when using our original data processing software as discussed in Sec. 6 below.

6. DATA ANALYSIS

A prototype version of the data processing code capable of processing 2D surface topography data recorded with CWI metrology was developed and successfully tested. The capabilities of the code have already been exploited to verify the dependence of the NASA GSFC CWI tool's ITF on the focus settings and the difference of the optimal focus setting for the vertical and horizontal directions has been observed (see also Sec. 2.5, above).

We treat the data measured with the developed HR BPRA test sample (Sec. 2.5) using the NASA GSFC Fizeau interferometer equipped with an additional cylindrical lens (Figure 13). Figure 17 presents the set of the profile plots corresponding to the masked area depicted in the inset. The CWI data pixel size is estimated assuming that the masked area is 20 x 20 mm (see the corresponding discussion in Sec. 2.

The 2D PSD distributions evaluated over the cropped areas in Figure 17b are shown in Figure 18. The 2D PSD distributions have rectangular shape that reflects the fact that the CWI data are sampled with rectangular pixels. Correspondingly, the 1D PSD distributions in the horizontal and vertical directions have different cutoff frequencies (Figure 19). The correct presentation and processing of the non-square-pixel data is an important feature of the upgraded software prototype.
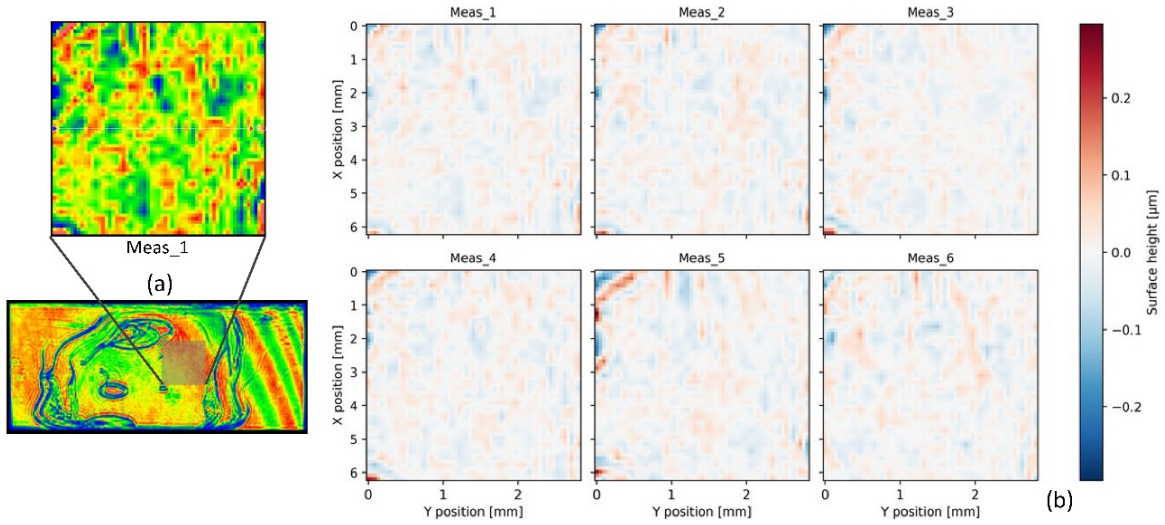
Figure 17. (a) The arrangement of the masked area used for cropping of the CWI calibration data with the ZYGO^{TM} Mx software and (b) the profiles of the cropped data generated with the developed software prototype.
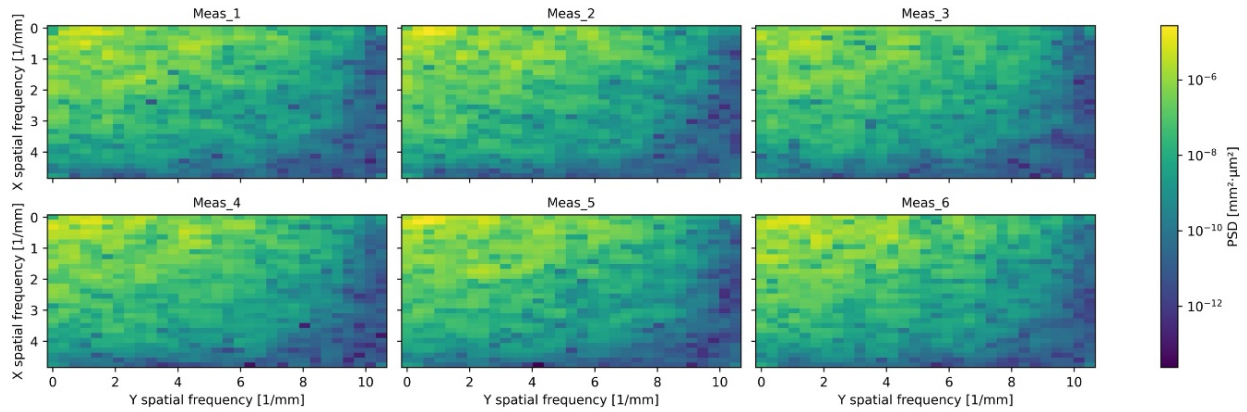

Figure 18. The 2D PSD distributions evaluated for the height profiles measured with the GSFC CWI tool.
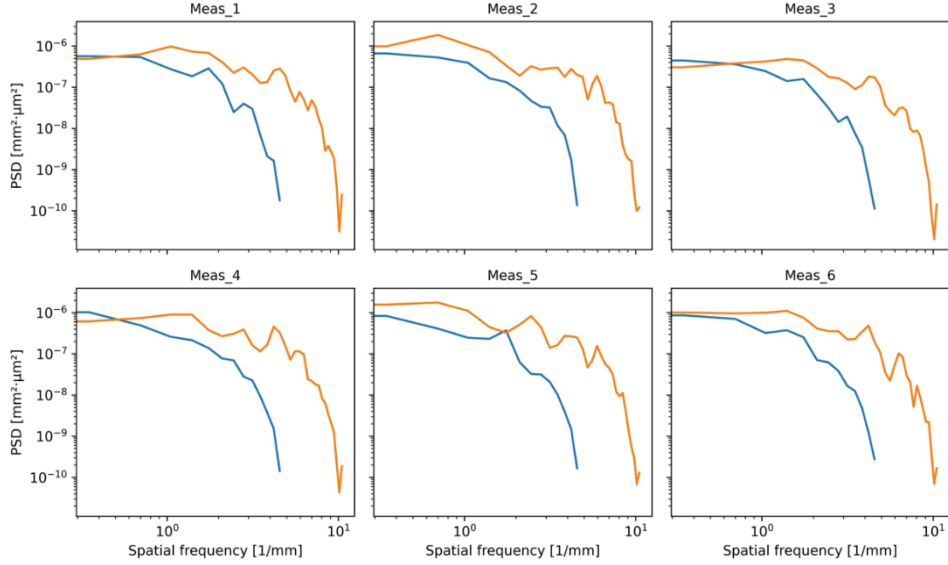
Figure 19. The averaged 1D PSDs distributions in the horizontal (the orange lines) and in the vertical (the blue lines) directions. Note that our software is capable for the processing of the data sampled with non-square pixels.

7. CONCLUSIONS

The major result of the investigations discussed throughout the present paper is a proof-of principle demonstration of the feasibility of application of the ITF calibration technique based on the BPRA test samples to the Fizeau interferometers with a cylindrical wavefront.

With a fabrication process developed to manufacture BPRA artifacts onto cylindrical substrates, two prototype samples have been fabricated. The samples have been used for the proof-of-principle test measurements with the Fizeau interferometer equipped with an additional cylindrical lens available at the NASA GSFC metrology laboratory.

For the data processing, we use an original prototype code capable of processing 2D surface topography data recorded with CWI metrology with a significantly different effective pixel size in the vertical (along the cylindrical lens axis) and horizontal directions.

A noticeable result of the measurements is the observed difference of the 1D PSD distributions in the vertical and horizontal directions that is an indication of an astigmatism of the system with different position of the foci in the vertical and horizontal directions. This observation can be thought of as evidence of the problem with the CWI tool's design using the external cylindrical null lens.

The performed investigations have also revealed a problem with performing electron beam lithography on top of a non-planar surface. Electron beam lithography is normally a good choice as a high-resolution direct write technique. However, it appears to be a challenging task to get a high quality BPRA samples on highly-curved cylindrical substrates.

Therefore, as the next steps of the project, we are treating other promising approach based on the nanoimprint lithography. HighRI Optics, Inc. has extensive experience in nanoimprint lithography. We are also developing a technology for fabrication of the calibration artifacts on deformable plane substrates with following mechanical bending of the patterned substrate to a desired shape. This work ins in progress.

ACKNOWLEDGEMENTS

DISCLAIMER

This document was prepared as an account of work sponsored by the United States Government. While this document is believed to contain correct information, neither the United States Government nor any agency thereof, nor The Regents of the University of California, nor any of their employees, makes any warranty, express or implied, or assumes any legal responsibility for the accuracy, completeness, or usefulness of any information, apparatus, product, or process disclosed, or represents that its use would not infringe privately owned rights. Reference herein to any specific commercial product, process, or service by its trade name, trademark, manufacturer, or otherwise, does not necessarily constitute or imply its endorsement, recommendation, or favor by the United States Government or any agency thereof, or The Regents of the University of California. The views and opinions of authors expressed herein do not necessarily state or reflect those of the United States Government or any agency thereof or The Regents of the University of California.

REFERENCES

[1] M. Kanaoka *et al.*, "Figuring and smoothing capabilities of elastic emission machining for low-thermal-expansion glass optics," *J. Vac. Sci. Technol. B Microelectron. Nanom. Struct. Process. Meas. Phenom.*, vol. 25, no. 6, p. 2110, Dec. 2007, doi: 10.1116/1.2789440.

[2] M. Yabashi *et al.*, "Optics for coherent X-ray applications," *J. Synchrotron Radiat.*, vol. 21, no. Pt 5, p. 976, doi: 10.1107/S1600577514016415.

[3] S. Yokomae, H. Motoyama, and H. Mimura, "Development of figure correction system for inner surface of ellipsoidal mirrors," *Precis. Eng.*, vol. 53, pp. 248–251, Jul. 2018, doi: 10.1016/J.PRECISIONENG.2018.04.010.

[4] V. V. Yashchuk *et al.*, "Investigation on lateral resolution of surface slope profilers," *Proc. SPIE 11109, 111090M/1-19, Sep. 2019*, p. 28, Sep. 2019, doi: 10.1117/12.2539527.

[5] K. Yamauchi *et al.*, "Microstitching interferometry for x-ray reflective optics," *Rev. Sci. Instrum.*, vol. 74, no. 5, p. 2894, Apr. 2003, doi: 10.1063/1.1569405.

[6] V. V. Yashchuk, S. Rochester, I. Lacey, and S. Babin, "Super-resolution surface slope metrology of x-ray mirrors," *Rev. Sci. Instrum.*, vol. 91, no. 7, p. 075113, Jul. 2020, doi: 10.1063/5.0005556.

[7] G. Gao, J. Lehan, W. Zhang, U. Griesmann, J. Soons "Computer-generated hologram cavity interferometry test for large x-ray mirror mandrels: design," Opt. Eng. 48(6), 063602 (2009); https://doi.org/10.1117/1.3153303.

[8] D. A. Content *et al.*, "Optical metrology for the segmented optics on the Constellation-X spectroscopy x-ray telescope," *UV Gamma-Ray Sp. Telesc. Syst.*, vol. 5488, p. 272, Oct. 2004, doi: 10.1117/12.553231.

[9] G. Gao, J. Lehan, U. Griesmann, "Dual-CGH interferometry test for x-ray mirror mandrels," Proc. SPIE 7389, 73891B (2009) https://doi.org/10.1117/12.830659.

[10] K. Munechika *et al.*, "Binary pseudo-random array test standard optimized for characterization of interferometric microscopes," *Proc. SPIE 11817*, p. 6, Aug. 2021, doi: 10.1117/12.2594995.

[11] V. V. Yashchuk *et al.*, "Calibration of the modulation transfer function of surface profilometers with binary pseudorandom test standards: expanding the application range to Fizeau interferometers and electron microscopes," *Opt. Eng.*, vol. 50, no. 9, p. 093604, Sep. 2011, doi: 10.1117/1.3622485.

[12] V. V. Yashchuk *et al.*, "Characterization and operation optimization of large aperture optical interferometers using binary pseudorandom array test standards," *Proc. SPIE 10749, 107490R/1-13*, Aug. 2018, doi: 10.1117/12.2322011.

[13] V. V. Yashchuk, S. Babin, S. Cabrini, W. Chao, U. Griesmann, I. Lacey, S. Marchesini, K. Munechika, C. Pina-Hernandez, and A. Roginsky, "Binary pseudorandom array test standard optimized for characterization of large field-of-view optical interferometers," Proc. SPIE 11490, 114900W/1-8 (2020); doi: 10.1117/12.2568309.

[14] V. V. Yashchuk, W. R. McKinney, and P. Z. Takacs, "Binary pseudorandom grating standard for calibration of surface profilometers," *Opt. Eng.*, vol. 47, no. 7, p. 073602, Jul. 2008, doi: 10.1117/1.2955798.

[15] S. K. Barber *et al.*, "Binary pseudo-random gratings and arrays for calibration of modulation transfer functions of surface profilometers, Nucl," *Instrum. Methods Phys. Res. Sect. Accel. Spectrometers Detect. Assoc. Equip*, vol. 616, pp. 172–182, doi: 10.1016/j.nima.2009.11.046.

[16] V. V. Yashchuk *et al.*, "Characterization of electron microscopes with binary pseudo-random multilayer test samples," *Nucl. Instruments Methods Phys. Res. Sect. A Accel. Spectrometers, Detect. Assoc. Equip.*, vol. 649, no. 1, pp. 150–152, Sep. 2011, doi: 10.1016/J.NIMA.2010.11.124.

[17] K. Kinnstaetter, A. W. Lohmann, J. Schwider, and N. Streibl, "Accuracy of phase shifting interferometer," Appl. Opt. 27, 5082-5089 (1988); https://doi.org/10.1364/AO.27.005082.

[18] C. Huang, "Propagation errors in precision Fizeau interferometry," 32(34), 7016-7021 (1993); https://doi.org/10.1364/AO.32.007016.

[19] L. Deck and C. Evans, "High performance Fizeau and scanning white-light interferometers for mid-spatial frequency optical testing of free-form optics," Proc. SPIE 5921, 59210A (2005); doi: 10.1117/12.616874.

[20] C. Kreischer, "Retrace error: interferometry's dark little secret," Proc. SPIE 8884, 88840X (2013); doi: 10.1117/12.2029324.

[21] I. Lacey, K. Anderson, G. P. Centers, R. D. Geckeler G. S. Gevorkyan, A. Just, T. Nicolot, B. V. Smith, and V. V. Yashchuk, "The ALS OSMS – Optical Surface Measuring System for high accuracy two-dimensional slope metrology with state-of-the-art x-ray mirrors," Proc. SPIE 10760, 1076002/1-20 (2018); doi: 10.1117/12.2321347.

[22] V. V. Yashchuk, N. A. Artemiev, I. Lacey, W. R. McKinney, and H. A. Padmore, "Advanced environmental control as a key component in the development of ultra-high accuracy ex situ metrology for x-ray optics," Opt. Eng. 54(10), 104104/1-14 (2015); doi: 10.1117/1.OE.54.10.104104.

[23] R. Su, Y. Wang, J. Coupland, and R. Leach, "On tilt and curvature dependent errors and the calibration of coherence scanning interferometry," Opt. Exp. 25(4) 3297-3310 (2017); https://doi.org/10.1364/OE.25.003297.

[24] P. L. Ruben, "Refractive null correctors for aspheric surfaces," App. Opt. 15(12), 3080-3083 (1976); https://doi.org/10.1364/AO.15.003080

[25] J. Lehan, T. Hadjimichael, D. Content, and W. Zhang, "Design and fabrication of refractive nulls for testing the segmented mirrors of the Constellation-X spectroscopy x-ray telescope (SXT)," Proc. SPIE 5900, 59001D (2005); doi: 10.1117/12.615316.

[26] R. Petre, D. A. Content, J. P. Lehan, S. L. O'Dell, S. M. Owens, W. A. Podgorski, J. Stewart, and W. W. Zhang, "The Constellation-X Spectroscopy X-ray Telescope," Proc. SPIE 5488, 505-514 (2004); doi: 10.1117/12.552062.

[27] M. Guainazzi, R. Willingale, L. W. Brenneman, E. Bulbul, J.-W. A. den Herder, E. Kuulkers, J.-U. Ness, and L. Natalucci, "On the scientific impact of the uncertainties in the Athena mirror effective area ," J. Astron. Telesc. Instrum. Syst. 8(4), 044002 (2022); https://doi.org/10.1117/1.JATIS.8.4.044002.

[28] V. V. Yashchuk, I. Lacey, and M. Sanchez del Rio, "Analytical expressions of the surface shape of 'diaboloid' mirrors," Proc. SPIE 11493, 114930N/1-13 (2020); doi: 10.1117/12.2568332.

[29] V. V. Yashchuk, K. A. Goldberg, I. Lacey, W. R. McKinney, M. Sanchez del Rio, and H. A. Padmore, "Diaboloidal mirrors: Algebraic solution and surface shape approximations," J. Synchrotron Rad. 28(4), 1031-1040 (2021); http://doi.org/10.1107/S1600577521004860.

[30] Lambda/DIOPTIC, "DIOPTIC DTC Diffractive Transmission Cylinder," https://www.lambdaphoto.co.uk/dioptic-dtc-diffractive-transmission-cylinder.html.

[31] G. D. Boreman, "Modulation Transfer Function in Optical and Electro-Optical Systems," Modul. Transf. Funct. Opt. Electro-Optical Syst., Mar. 2010, doi: 10.1117/3.419857.

[32] S. K. Barber et al., "Stability of modulation transfer function calibration of surface profilometers using binary pseudo-random gratings and arrays with nonideal groove shapes," Opt. Eng., vol. 49, no. 5, p. 053606, May 2010, doi: 10.1117/1.3431659.

[33] V. V. Yashchuk, K. Munechika, S. Rochester, W. Chao, I. Lacey, C. Pina-Hernandez, and P. Z. Takacs, "Reliability investigation of the instrumentation transfer function calibration technique based on binary pseudo-random array standards," SPIE Proc. 12240, 122400D/1-11 (2022); doi: 10.1117/12.2633476.